ASTRO-F/FIS Observing Simulation:
Detection Limits for Point Sources

Woong-Seob JEONG[1], Soojong PAK[1,2,3], Hyung Mok LEE[1], Takao NAKAGAWA[3], Jungjoo SOHN[1], Insun AHN[1], Issei YAMAMURA[3], Masaru WATANABE[3], Mitsunobu KAWADA[4] and Hiroshi SHIBAI[4]

[1]*Astronomy Program in Graduate School of Earth and Enviromental Sciences,*
Seoul National University, Shillim-Dong, Kwanak-Gu, Seoul 151-742, South Korea
jeongws@astro.snu.ac.kr, soojong@astro.snu.ac.kr, hmlee@astro.snu.ac.kr,
jjsohn@astro.snu.ac.kr, ais@astro.snu.ac.kr
[2]*Korea Astronomy Observatory, Whaam-Dong, Youseong-Gu, Taejeon 305-348, South Korea*
[3]*Institute of Space and Astronautical Science, Yoshinodai 3-1-1, Sagamihara, Kanagawa 229-8510, Japan*
nakagawa@ir.isas.ac.jp, yamamura@ir.isas.ac.jp, watanabe@ir.isas.ac.jp
[4]*Graduate School of Science, Nagoya University, Furo-cho, Chigusa-ku, Nagoya 464-8602, Japan*
kawada@u.phys.nagoya-u.ac.jp, shibai@phys.nagoya-u.ac.jp

Abstract

We describe the observing simulation software FISVI (FIS Virtual Instrument), which was developed for the Far-Infrared Surveyor (FIS) that will be on the Japanese infrared astronomy mission ASTRO-F. The FISVI has two purposes: one is to check the specifications and performances of the ASTRO-F/FIS as a whole; the other is to prepare input data sets for the data analysis softwares prior to launch. In the FISVI, special care was taken by introducing the "Compiled PSF (Point Spread Function)" to optimise inevitable, but time-consuming, convolution processes. With the Compiled PSF, we reduce the computation time by an order of magnitude. The photon and readout noises are included in the simulations. We estimate the detection limits for point sources from the simulation of virtual patches of the sky mostly consisting of distant galaxies. We studied the importance of source confusion for simple power-law models for $N(> S)$, the number of sources brighter than S. We found that source confusion plays a dominant role in the detection limits only for models with rapid luminosity evolution for the galaxy counts, the evolution of which is suggested by recent observations.

Key words: methods: data analysis — techniques: image processing — galaxies: photometry — infrared: galaxies

Table 1. Specifications of the FIS.

Band	Wavelength range (μm)	Array size (pixel)	Pixel size (arcsec)	Pitch size (arcsec)	Sampling rate (Hz)
WIDE-L	$110 - 200$	15×3	44.2	49.1	15.2
N170	$150 - 200$	15×2	44.2	49.1	15.2
WIDE-S	$50 - 110$	20×3	26.8	29.5	22.8
N60	$50 - 75$	20×2	26.8	29.5	22.8

1. Introduction

The FIS (Far-Infrared Surveyor) is one of the focal plane instruments of the ASTRO-F mission (previously known as IRIS) (Murakami 1998; Shibai 2000; Nakagawa 2001). The ASTRO-F satellite will be launched into a sun-synchronous orbit at an altitude of 750 km, which corresponds to an orbital period of 100 min. The telescope, which is cooled down to 5.1–5.8 K, has a 67 cm primary mirror. The major task of this mission is to carry out an all-sky survey across the 50–200 μm range. The basic parameters of the ASTRO-F/FIS are summarized in table 1 (see also Kawada 2000).

ASTRO-F/FIS will bring data with much higher sensitivity and angular resolution than those of IRAS (see Kawada 2000 for detailed comparison). Such data sets will be of great value for many areas of astrophysics, including cosmology, galaxy evolution, interstellar medium, and asteroids.

Generally speaking, the hardware characteristics of each component in a space mission can be measured in the laboratory. However, it is very difficult to make end-to-end tests of a mission in the laboratory. Hence, based on data measured for each component, numerical simulations are frequently used to understand the instrument performances as a whole (e.g., Garcia et al. 1998; Boggs, Jean 2001). Moreover, the complicated interplay between the celestial sources and hardware specifications can be studied only by a simulation prior to the launch.

We have constructed a software simulator called the FISVI representing Virtual Instrument of the FIS, that can simulate the data stream of ASTRO-F/FIS (Jeong et al. 2000). This work is an extension of initial work by Matsuura et al. (2001). The purposes of the FISVI are : (1) to confirm the performance of the hardware as a whole and (2) to generate simulated FIS survey data sets as inputs for data-reduction software prior to launch.

One of the key questions regarding the performance of ASTRO-F is the effective detection limit for faint sources. Depending on the size of the sources compared to the beam size of ASTRO-F, the source can be either extended or point-like, and the detection limits depend on the nature of the sources. In the present work, we only consider point sources.

There are several factors contributing to the detection limits. The sensitivity of the

detectors and the entire telescope system allows only sources brighter than a certain threshold to be reliably measured. Since the photons follow Poisson statistics, the background photons due to the sky brightness as well as the telescope emission should fluctuate, and a meaningful detection of a source can be made only if the signal from the source exceeds the level of the fluctuations. The sky confusion noise by the cirrus emission causes an uncertainty in the determination of the source flux, due to the variation of the sky brightness (Herbstmeier et al. 1998; Kiss et al. 2001). The readout process also adds more fluctuations. Moreover, the measurement of the brightness of a source can be further influenced by neighboring sources if more than one source lies within a single beam of the telescope. The final detection limit should thus depend on the performance of the entire system, the brightness of sky and telescope emission, readout process, and the distribution of sources as a function of the flux.

There have been a number of estimates of detection limits based on the available laboratory data (e.g., Kawada 1998, 2000) using simple calculations. Clearly, a more realistic estimation can be made by using numerical simulations. In the present work, we carried out simulations of the ASTRO-F/FIS observations under several different circumstances in order to obtain still more reliable detection limits which can be used to design scientific projects.

The present paper is organised as follows. In section 2, we briefly describe the design and the structure of the FISVI. In section 3, we explain how we obtain the observed images based on the simulated data set. In section 4, we make estimate on the detection limits of the ASTRO-F/FIS under various circumstances. First, we estimate the detection limits of a single isolated point source while considering only photon and readout noises. Also, we estimate the confusion noise (Condon 1974; Franceschini et al. 1989) for distributed sources using a simple formula. By carrying out aperture photometry to the simulated images, we finally obtain combined detection limits that include photon, readout, and confusion noises. The final section summarises our conclusions.

2.   Structure of FISVI Software

The algorithm of the FISVI software is shown in figure 1. The input data file provides the coordinates and fluxes of the sources in the sky. Although the sources would appear either point-like or extended, we concentrate on point sources in this paper. The software first makes images on the focal plane by convolving the point sources and the Point Spread Function (PSF) of the telescope and the instrument. The software generates time-series data for each pixel by simulating the scanning procedure of the ASTRO-F/FIS survey mode observations.

Since the PSF, the filter transmission, and the detector response depend on the wavelength of incoming photons, we need to do repeated calculations (procedures boxed in the left panel of figure 1) for different wavelengths within the individual FIS bands, as shown in the left panel of figure 1. To elude this and speed up the procedure, we introduce the Compiled PSF in this work, with which we can perform this scanning procedure at once, as shown in the

3

Fig. 1. Flow charts of FISVI. The left chart shows a straightforward procedure based on the realistic photon path, where repeated calculations would be necessary over the wavelength grids ("λ Convolution"). The right chart, on the other hand, shows the accelerated algorithm using the Compiled PSF for the FISVI.

simplified flow chart in the right panel of figure 1. A more detailed discussion on the gains in the computational time and possible errors due to the use of the Compiled PSF are presented in appendix 1.

The readout values for each pixel are represented by a series of integrated charges taken over the area covered by the pixel, sampled at regular time intervals. The integrated charges are set to zero at every reset interval. The time series of the integrated charges are differentiated to obtain the charges accumulated during the sampling interval (see appendices 2 and 3 for detailed process). We also generate the photon and readout noise and include them to be part of readout values. A more detailed discussion on the implementation of noise is presented in

4

subsection 4.1. The time-series data are converted into the brightness distribution on the sky, and are used to reconstruct the images, as described in section 3.

3. Image Reconstruction

The FISVI generates time-series data for each pixel. In figure 2, we show a series of readout values of a pixel that scans across a point source. No reset was applied during the readout sequence shown in this figure because the reset time interval is usually much longer than the passage of a Compiled PSF over a point source. The differentiation (subtraction of adjacent sampling points) of this curve gives the signal obtained during a sampling interval by one detector pixel, which is shown in the lower panel of figure 2.

The pixel readouts can be used to reconstruct the images. In the current implementation of the FISVI, following method was used to generate the image. In order to reconstruct the image, we assume that pixel value represents the uniform intensity over the pixel surface. This means that a particular point can be covered by more than one readout. We always take the average values of multiple readouts in order to construct images (see figure 3). Due to the convolution of the image with the pixel size, the output image will be blurred slightly.

4. Estimations of FIS Performance

An estimation of the detection limits for the planned mission is very important. For ASTRO-F, the detection limits were estimated by using analytic methods (Kawada 1998, 2000). In the present work, we made a numerical estimate for a single point source using the latest information for the detectors and filters, and compared them with the photometric results on the FISVI generated images that contain a large number of point sources.

4.1. Detection Limits for a Single Point Source

The detection limits for a single point source depend on the level of noise. There are several sources of noise: photon noise due to the sky background and thermal emission from the telescope, and readout noise. The sky background varies significantly from place to place in the sky. On average, the infrared sky becomes brighter in the Galactic plane, and diminishes toward the Galactic poles. Within the Galactic plane, the emission from the Galactic center direction appears to be brighter than towards the anti-center direction. Because of thermal emission by interplanetary dust particles, the ecliptic plane is also brighter than the ecliptic pole region. In figure 4, we show the assumed surface brightness distribution of background emissions from the interstellar dust, the interplanetary dust and the telescope, for the purpose of generating photon noises. These background emissions from the sky are assumed to correspond to the dark part of the sky and the sky confusion noise due to the structure of the cirrus emission is not considered. The telescope temperature is assumed to be 6 K, as a conservative number. In figure 4, we also plotted the thermal emission from the 6.5 K telescope as a comparison.
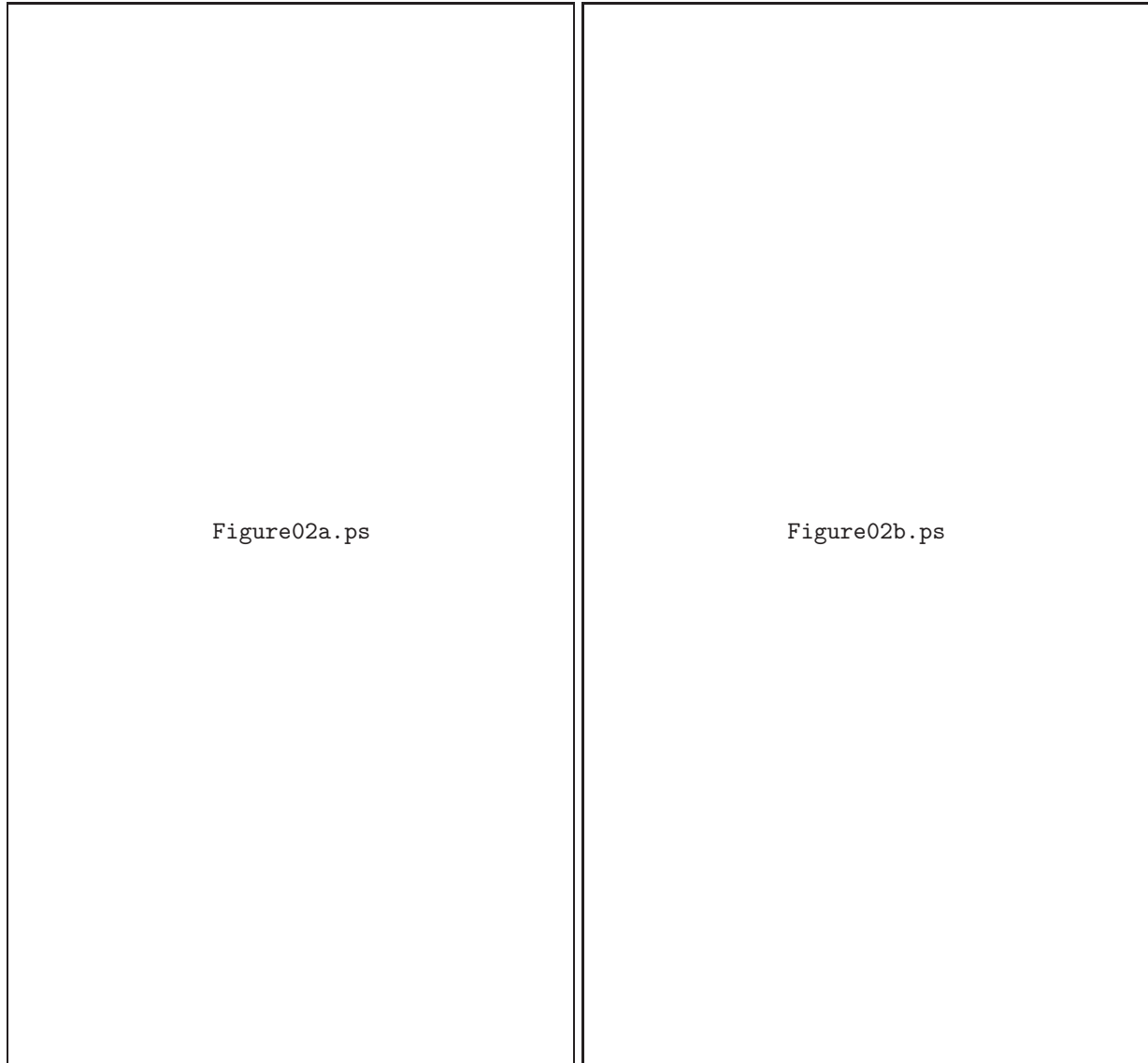
Figure02a.ps

Figure02b.ps

Fig. 2. Example of a series of readout values, which corresponds to the integrated charges since the last reset [see equation (A5)], of a WIDE-L pixel that scans through a point source (left panel). The differentiation of the integrated charges as shown in the right panel corresponds to the signal obtained during a sampling interval by one detector pixel passing the image of a point source. The sampling interval was $14.''2$, corresponding to the 15.2 Hz readout (see table 1).
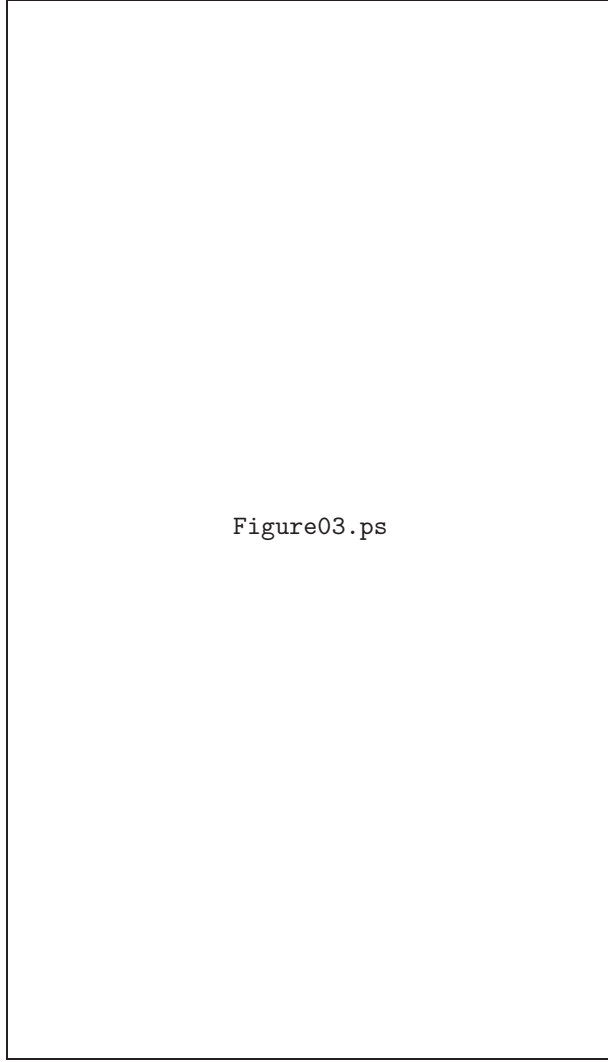
Fig. 3. Schematic figure for image reconstruction by pixel averages. At any given point, we take the average of the pixel readouts that were covered by those pixels. In the figure, the darker area means the area that was covered more.

Evidently, the contribution from the telescope is smaller than that from the interplanetary or interstellar dust as long as the telescope temperature is lower than 6.5 K for the entire FIS bands. The sky brightness throughout the spectral region of the FIS varies from 5 to 7 MJy sr^{-1}. Obviously, we would need to apply a position-dependent background brightness for more realistic sky simulations, which affects the photon noise. The incoming photon stream on pixels due to background emission is assumed to follow Poisson statistics.

The readout circuit also generates uncertainties of the output values, called readout noise. This type of noise is independent of the sampling rate and the integration time, and we assumed the total noise in the effective bandwidth at the first stage of the field effect transistor (FET) gate to be 3 μV. In the simulation, we assumed that the readout noise follows Gaussian statistics.

Figure04.ps

Fig. 4. Assumed background emissions. We consider three components for the background emission, i.e., interstellar dust (dotted), interplanetary dust (dashed) and telescope emission assuming 6 K (dot-dashed line) or 6.5 K black body (long dot-dashed line). In our simulations, the telescope temperature is always assumed to be 6 K.

Table 2. Simple estimates of 5σ detection of single pixels and the ratios of photon-to-readout noises.

	5σ Det. Limit (mJy)*	$\sigma_{\mathrm{r}}/\sigma_{\mathrm{ph}}^{\dagger}$
WIDE-L	39	1.3
N170	76	1.8
WIDE-S	20	1.6
N60	52	2.5

* Average flux density in the bandwidth.

† Readout-to-photon noise ratio.

4.1.1. Simple estimation

The sky brightness throughout the spectral region of the FIS varies from 5 to 7 MJy sr^{-1}. The integrated photons fluctuate following the Poisson statistics while the readout process adds readout noise, which is assumed to follow Gaussian statistics. The r.m.s. fluctuation of voltage across the integrating charge due to readout noise can be converted to the fluctuation in the number of charges by

$$D_{\mathrm{rms}} = \frac{C\,V_{\mathrm{rms}}}{e}, \tag{1}$$

where C is the capacitance of the charge integrators [7 pF for SW (short wavelength) and 10 pF for LW (long wavelength) bands, respectively], and e is the elementary charge. The total noise is a combination of photon and readout noise.

If we assume that a single pixel detector receives the entire photon flux of the point source, we can obtain the accumulated charge during 'the effective integration time' that elapses until the detector pixel passes through one point. For a photoconductor, the noise by this photon flux arises from the sequence of generations and recombinations of photoelectrons. We calculated this generation-recombination noise (G-R noise), $I_{\mathrm{G-R}}$ (Rieke 1994) using

$$\langle I_{\mathrm{G-R}}^2 \rangle = 4e^2 \varphi \eta G^2 df, \tag{2}$$

where φ is the photon flux, η is the quantum efficiency, G is the photoconductive gain, and df is the effective bandwidth. We assumed that the source has the SED of a 40 K blackbody. The 5σ detection limits computed in this way for all FIS bands are shown in table 2. Also shown in this table is the relative importance of the photon and readout noise. In all cases, the readout noise is more important than the photon noise, with narrow bands (N170 and N60) being more dominated by readout noise.

4.1.2. Estimation using scanning simulations of a single pixel

We also estimate the detection limits from the detector scanning routines in the FISVI for a single pixel. The behavior of the readout values as a function of the sampling sequence is shown in figure 2. The contribution due to background can be obtained by subtracting the

Table 3. 5σ detection limits of FIS bands from scanning simulations with a single pixel.

	Detection Limits (mJy)
WIDE-L	40
N170	80
WIDE-S	20
N60	47

contribution from the source alone. The expected amount of the fluctuation is proportional to $G\sqrt{\varphi\eta}$ for a given span of the scanning period of t_1 to t_2 [see equation (2)]. The total amount of fluctuation of the readout value due to noises during the same scanning span, σ_{tot}, is

$$\sigma_{\mathrm{tot}} = \sqrt{\sigma_{\mathrm{ph}}^2 + \sigma_{\mathrm{r}}^2}, \tag{3}$$

where σ_{ph} and σ_{r} are the fluctuation due to the photon and readout noise, respectively. Here, we assume that the readout noise is always a constant while the amount of charge fluctuation due to the photon noise increases as $G\sqrt{\varphi\eta}$, as dictated by the Poisson nature. For a given brightness of a source, we can obtain the S/N ratio if we specify t_1 and t_2. Since the signal (photocurrent) and the photon noise are proportional to G, S/N depends on $\sqrt{\eta}$ on the condition that the photon noise is the dominant case. From equation (A7) and the assumption $G = 0.9$, we can obtain the quantum efficiency, η, as 0.17 for SW and 0.27 for LW detectors, respectively. The determination of t_2 and t_1 was done to maximize the S/N. We find that this can be done when we start the scanning at a distance of $2W_{\mathrm{H}}$ and continue until the same distance in the opposite side, where W_{H} is the full width at half maximum of the beam patterns (see subsubsection 4.2.2 for details). The 5σ detection limits determined in this way for all FIS bands are listed in table 3. These estimates also assume a blackbody source with a temperature of $40\,\mathrm{K}$. We find that the estimates using the simple method described in subsubsection 4.1.1 and here agree very well each other. The largest discrepancy occurs for the N60 band, where the estimated detection limit using scanning simulation is lower by around $10\,\%$. The instrumental noise in ISO observation is estimated to be 15–45 mJy (Herbstmeier et al. 1998; Dole et al. 2001). Assuming our background brightness of ~ 5 MJy sr^{-1}, this noise level is similar with our estimation in the wide bands. We analyse the photometric accuracy of point sources in more realistic simulations with distributed sources below.

4.2. Simulations with Distributed Point Sources and Realistic Detector Configurations

The FISVI takes into account the full configuration of FIS detector arrays. We now discuss the simulations over a finite patch of the sky with randomly distributed sources. By carrying out the photometry of simulated images, we should be able to determine more realistic detection limits.

Most faint sources to be observed by the ASTRO-F/FIS are expected to be distant galaxies. Since the size of the PSFs at far-infrared wavelengths is relatively large, we expect that the number of sources overlapped within a given PSF will be larger. In such a situation, the source confusion would be important for faint sources. In this section, we consider how the source confusion would affect the observations by the ASTRO-F/FIS.

4.2.1. Source distribution

The effect of confusion depends on the distribution of sources in the sky and the PSF. We assume that $N(>S)$, the number of sources whose flux is greater than flux S, as a power-law on S,

$$N(>S) = N_0(>S_0) \left(\frac{S}{S_0} \right)^{-\gamma}, \tag{4}$$

for $S_{\min} < S < S_{\max}$, where N_0 and S_0 are normalisation constants. For uniformly distributed sources in Euclidean space, γ is 1.5. If the galaxies experience strong luminosity evolution from active to less active star formation with time, γ will become greater than 1.5. The curved space could also give γ different from 1.5. The analysis of IR galaxy counts by ISO and SCUBA suggests that γ would be greater than 1.5 but lower than 2.5 at around ~ 150 mJy (Puget et al. 1999; Franceschini et al. 2001; Pearson 2001; Dole et al. 2001). Matsuhara et al. (2000) suggested that γ could be steeper than 2.5 based on the fluctuation analysis due to the strong evolution. In this paper, we examine three cases: $\gamma = 1.5$, 2.5, and 3.0. We fixed $S_{\min} = 10$ mJy throughout the paper. Since there is no divergence due to $S_{\max}$, we do not fix this number.

We need to specify the normalisation constants, N_0, at a given flux S_0, which is set to be 100 mJy. These constants are determined from IR galaxy counts normalised to Euclidean law $[N(>S) \propto S^{-1.5}]$ at 90 μm based on the IRAS survey and the European Large Area ISO Survey (Efstathiou et al. 2000; Franceschini et al. 2001). In the following cases, though the source count results are different for different bands and galaxy evolution, we assumed that there are 10 sources brighter than 100 mJy per square degree, i.e., $N_0(>100$ mJy$) = 10$, in every observational band and the SED of all sources are flat within a given FIS band. The number density of sources was estimated to be 316 per square degrees corresponding to 0.2 within a circle of radius of W_H in LW bands for $\gamma = 1.5$ with the above normalisation. The density becomes 10-times larger for the case of $\gamma = 2.5$ and the case of $\gamma = 1.5$ and $N_0 = 100$, and 19 times larger for the case of $\gamma = 3.0$ and $N_0 = 60$. We expect that source confusion becomes important for these distribution. The distribution of sources in the sky is assumed to be uniform Poisson. In this work, we want to check the pure confusion effect for the same distributed galaxies by excluding other factors, e.g., various types of SED, the redshift distribution, the luminosity function and the galaxy evolution. For a comparison, we also check other cases: the Euclidean space with a large normalisation constant ($N_0 = 100$) and an extreme case ($\gamma = 3.0$, $N_0 = 60$) (Matsuhara et al. 2000).

4.2.2. Simple estimate of the confusion noise

Although the clustering of sources could also affect the confusion noise, we ignore such a possibility for simplicity. Following Condon (1974) and Franceschini (1989), we obtain the noise due to confusion as

$$\sigma^2_{\text{confusion}} = \int_0^{x_c} x^2 R(x) dx, \tag{5}$$

where $x\ [= S\,h(\theta,\phi)]$ is the intensity, x_c is a cutoff value, and $R(x)$ is the mean number of sources within the normalised beam pattern, $h(\theta,\phi)$:

$$R(x) = \int_{\Omega_{\text{beam}}} n\left(\frac{x}{h(\theta,\phi)}\right) \frac{d\Omega}{h(\theta,\phi)}, \tag{6}$$

where $n(S)$ is a differential number count.

In this calculation, we use the beam pattern (see figure 5), which is obtained from a simulated image of an isolated point source using the FISVI without noises. The beam pattern obtained in this way is somewhat wider than the Compiled PSF due to pixel convolution. We also use the differential number count obtained from the same source distribution assumed in subsubsection 4.2.1. These considerations are for the purpose of comparing with the results from the photometry in subsection 4.3. We list the 5σ confusion noise in table 4, obtained by using equation (5) for $\gamma = 1.5$, $\gamma = 2.5$, and $\gamma = 3.0$. We also estimated the crowded fields for $\gamma = 1.5$ by simply increasing N_0 by a large factor, i.e., $N_0(> 100 \text{ mJy}) = 100$. The 5σ confusion noise is the same for the wide and narrow bands, because the beam patterns are similar for two bands. Because of differences in the size of beam profiles between long and short wavelengths, the detection limits for LW are higher than those of SW bands. The detection limit by confusion is approximately proportional to $N_0^{1/\gamma}$.

The confusion noise in FIRBACK survey by ISO is estimated to be around $\sigma_c \simeq 45$ mJy (Dole et al. 2001). In our case, we used the slope of the source distribution as $\gamma = 1.5$ or $\gamma = 2.5$ and set the normalisation constant as $N_0(> 100 \text{ mJy}) = 10$ by using the 90 μm source count result (Efstathiou et al. 2000). Though the slope of the source count by Dole et al. (2001) is similar to the Euclidean space ($\gamma = 1.5$), the normalisation constant should be different because the source density and the galaxy evolution is different in other bands. Therefore, these discrepancies result from the different normalisation and the cutoff flux ($S_{\text{min}} = 10$ mJy).

4.3. Realistic Simulations

The assumed source distribution of equation (4) can be used to simulate the observed sky by the ASTRO-F/FIS. By analysing the simulated images, we can address the effects of the various sources of noises to the observation in a more realistic way.
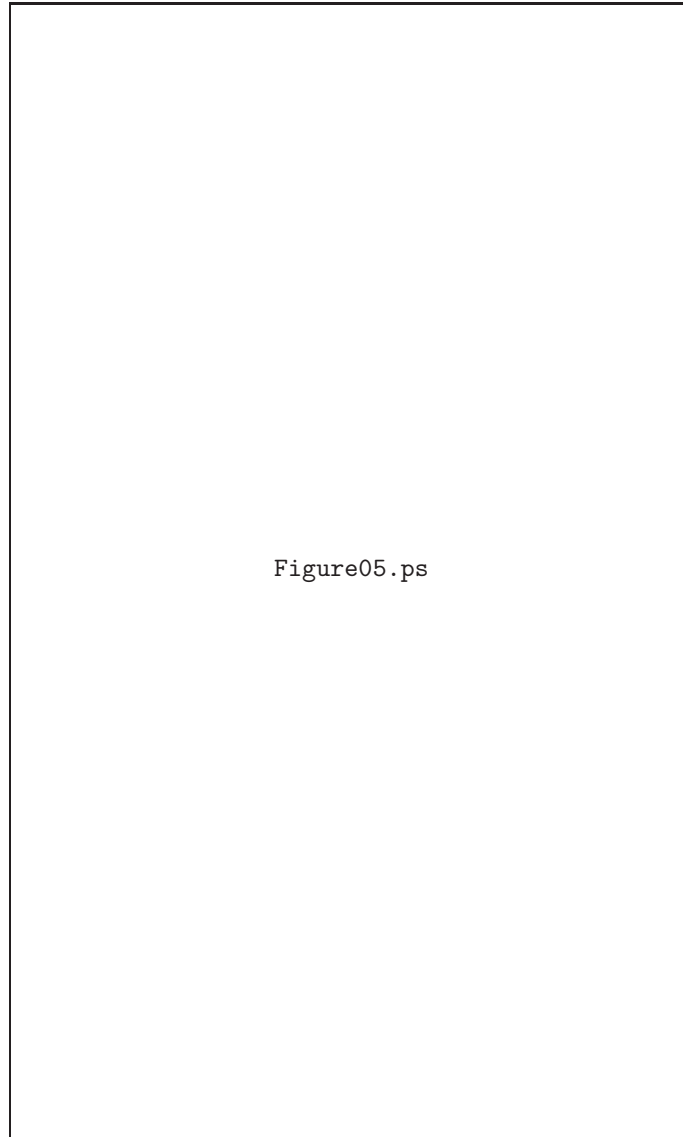
12

Figure05.ps

Fig. 5. Comparison between the Compiled PSF (dotted) and the beam pattern (solid line) used in calculating the theoretical confusion (WIDE-L). Because we assumed a flat SED for all sources in this simulation, we used one Compiled PSF in the PSF-convolution.

Table 4. 5σ detection limits due to confusion noise based on theoretical estimates.

Band	$\gamma = 1.5$ $N_0^* = 10$ (mJy)	$\gamma = 1.5$ $N_0^* = 100$ (mJy)	$\gamma = 2.5$ $N_0^* = 10$ (mJy)	$\gamma = 3.0$ $N_0^* = 60$ (mJy)
WIDE-L	23	108	50	196
N170	24	115	52	204
WIDE-S	12	54	35	123
N60	11	52	34	121

* $N_0(> 100\,\mathrm{mJy})$. Number per square degree.

4.3.1. Realistic simulations

Using the FISVI, we generated two-dimensional images in the FIS bands for two different virtual sky data with different γ. We made two different sets of simulations. One was with the noise levels described in earlier in this section; the other was with the noise reduced to almost a negligible level in order to separate the effects of confusion. The image size for the distributed source simulation is $8192'' \times 8192''$. As mentioned in the previous section, we expect that the confusion is important, especially for the cases that γ is greater than 2.5. In figure 6, we show an example of the simulated images with the normal level of noise.

We carried out aperture photometry on the simulated images using SExtractor software $v2.0.0$ (Bertin, Arnouts 1996). Some influential parameters were optimised for better detection of the source, while the remaining were left intact as default values. We set the threshold in the source detection and the analysis as 3, the size of the photometric aperture as FWHM of beam pattern, and we did not apply a filter for detection. In order to calibrate the output flux, we used the five brightest input sources.

Figure 7 shows the distribution of the $S_{\mathrm{out}}/S_{\mathrm{in}}$ as a function of S_{in}, where S_{in} and S_{out} denote the input flux and the flux obtained by photometry. In the upper-left panel of figure 7, we assumed that it is for the case with $\gamma = 1.5$ and $N_0 = 10$, and negligible contribution of photon and readout noise. We also assumed that detected source corresponds to the input source if the position of the detected source lies within $9''$ for SW bands and $15''$ for LW bands from the input source location. We found very good correlation between the input and output fluxes, and hence can conclude that the confusion noise is also negligible for this case.

The noise added results for the case with $\gamma = 1.5$ are shown in the upper-left panel of figure 8. The flux uncertainty becomes significant near the estimated detection limits due to photon and readout noise. Below the detection limit, most of the detected sources have an output flux greater than the input flux: This is simply because detection can be possible only when positive noises have been added to the source.

The results with more crowded sources (i.e., $\gamma = 2.5$ and $\gamma = 3.0$) are shown in the lower
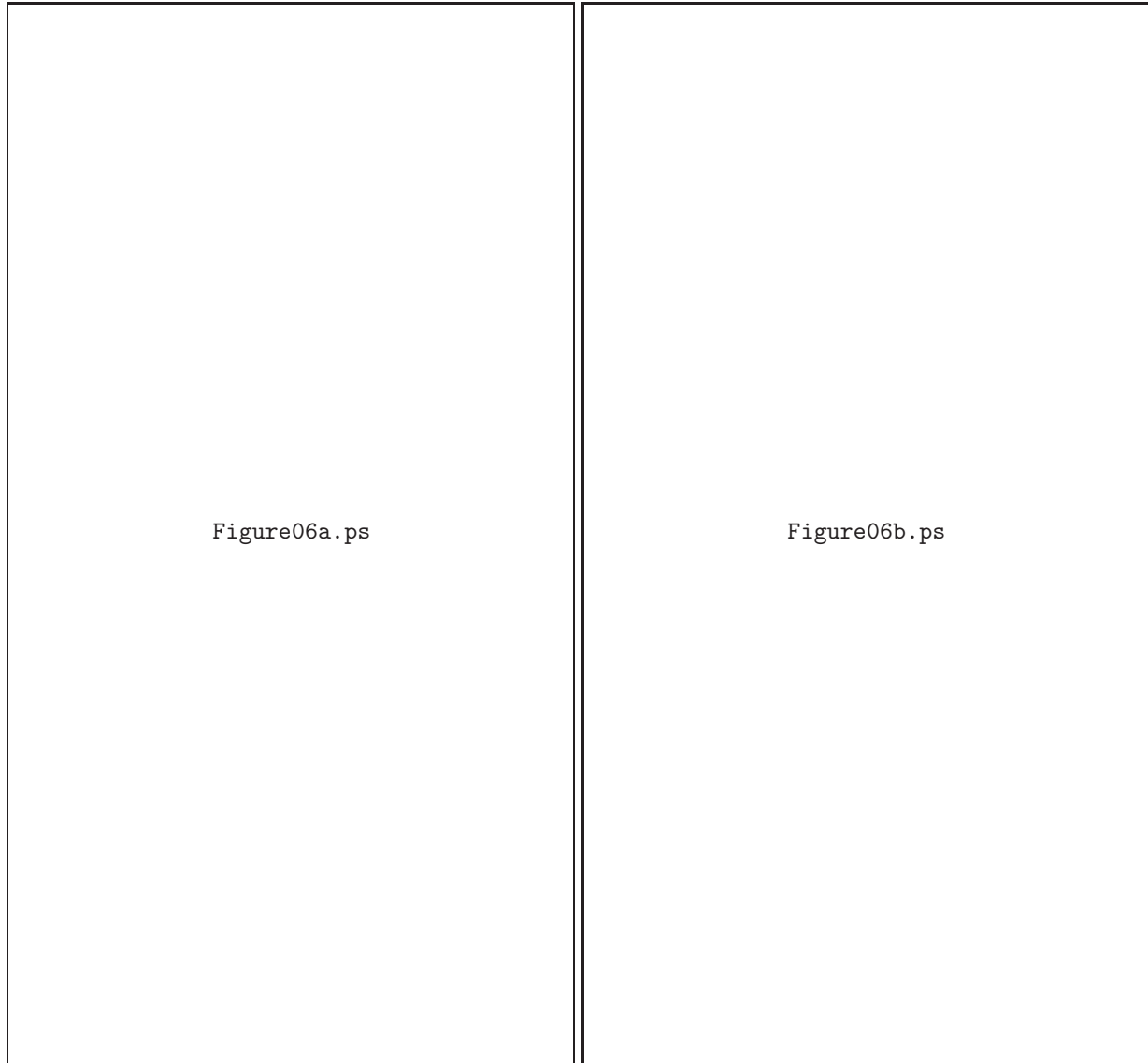
14

Figure06a.ps

Figure06b.ps

Fig. 6. Simulated images in the WIDE-L band for distributed sources. We generated the distributed sources according to the cases of $\gamma = 1.5$ and $N_0 = 10$ (left panel) and $\gamma = 2.5$ and $N_0 = 10$ (right panel). Photon and readout noises are added in these images.

Figure07a.ps

Figure07b.ps

Figure07c.ps

Figure07d.ps

Figure08a.ps

Figure08b.ps

Figure08c.ps

Figure08d.ps

panels of figure 7 for negligible noises, and figure 8 for normal noises. Even with negligible noises, we find that there are large deviations of the output fluxes from the input fluxes. Thus, the flux uncertainties are mostly caused by the source confusion shown in figure 7. Similar to the case dominated by the photon and readout noise shown in the upper-right panel of figure 8, S_{out} is systematically overestimated for sources below the theoretical confusion limits. Such an upward bias was caused by source confusion; many of the detected sources contain fainter sources within the beam. Actually, the significant upward bias is partially due to the parameter, i.e., threshold, set in SExtrator. First, SExtractor estimates the background fluctuation from each local area. Because we reduce the noise below a negligible level, the calculated background fluctuations are mainly due to many dim sources. The detected sources at low flux surely have a flux above the fluctuation times the threshold; these detected sources cause a significant upward bias. In the case of heavy confusion, the trend of the boosted flux (see the lower panels of figure 8) is very similar to the case without noises (see the lower panels of figure 7), which means that the faint sources work as the dominant noise.

Figure 9 shows the integrated source count results. For a comparison, we also plot the input source distribution. In the case of weak source confusion (i.e., $\gamma = 1.5$ and $N_0 = 10$) (upper-left panel of figure 9), the source count from a simulated image follows the input source distribution well, except for the faint ends dominated by photon and readout noise. However, the lower panels of figure 9 show that the source distribution deviated from the input one due to source confusion. The location of the estimated confusion limit of table 4 is also shown in this figure. The observed slope is significantly different from the input slope. The output slope can be 1.5-times larger than the input slope in the case of a crowded source distribution.

As we mentioned in subsubsection 4.2.2, we generated crowded fields for the case of $\gamma = 1.5$ by simply increasing N_0 by a large factor, i.e., $N_0(> 100 \text{ mJy}) = 100$ and the case of $\gamma = 2.5$ and $N_0 = 10$, to exclude photon and readout noise in order to check the effect of pure source confusion. Because there are no significant difference between the case with and without the photon and readout noise, as can be seen in the upper-right panel of figures 7 and 8, we show the source count result with the photon and readout noise in the upper-right panel of figure 9 in comparison with the less-crowded case (upper left). Clearly, the confusion becomes important at around $S = 100$ mJy for WIDE-L according to a theoretical calculation, but the slope does not change. The change in the slope appears to occur only when the underlying $N(> S)$ varies rather steeply on S. The lower-right panel of figure 9 shows the case of $\gamma = 3.0$ and $N_0 = 60$, including the photon and readout noise. The slope of the source count is significantly changed by the heavy confusion, and the source detection mainly depends on source confusion.

4.3.2. Detection limits from simulations

It is not easy to define the detection limits from the simulated data. Since the detection becomes increasingly difficult for sources below the detection limits, we first define the 'detection

Figure09a.ps

Figure09b.ps

Figure09c.ps

19

Figure09d.ps

Table 5. Detection limits for distributed point sources without photon and readout noise.

Band	$\gamma = 1.5$ $N_0^* = 10$ (mJy)	$\gamma = 1.5$ $N_0^* = 100$ (mJy)	$\gamma = 2.5$ $N_0^* = 10$ (mJy)	$\gamma = 3.0$ $N_0^* = 60$ (mJy)
WIDE-L	no confusion	100	58	355
N170	no confusion	105	61	390
WIDE-S	no confusion	45	31	305
N60	no confusion	40	30	278

* $N_0(> 100\,\mathrm{mJy})$. Number per square degree.

correctness' such that the ratio of the number of correctly detected sources to the number of detected sources from the photometry. We assume that the flux of the correctly detected source is the measured flux from the photometry, and agrees with the input flux within a 20% error. The detection correctness can be near unity for sources well beyond the detection limit, and goes down rapidly below the detection limit. We find that the detection correctness reaches around 0.7 at the estimated detection limit of a single scan. We thus define the location of the 70% detection correctness as the detection limit in our simulated data.

Figure 10 show a plot of the detection correctness with the photon and readout noise. We first attempted to estimate the detection limit purely due to source confusion. We arbitrarily suppressed the photon and readout noise by a factor of 100 so that the noise-dominated detection limit would become much less than the lower limit of the source flux of 10 mJy. The resulting detection limits, estimated based on the detection correctness, are summarized in table 5. Under this condition, because the source detection is affected by the source confusion and the photometric accuracy, we could obtain similar detection limits in both narrow and wide bands. These numbers are similar to those in table 4, except for $\gamma = 1.5$, where the detection correctness remains larger than 0.7, even for the faintest sources and for the case of the crowded source distribution. This means that the confusion is not important for $\gamma = 1.5$ and $N_0(> 100$ mJy$) = 10$.

Table 6 shows the estimates of combined detection limits where the readout noise, the photon noise, and the confusion noise are considered. Since the confusion is not important for the case of $\gamma = 1.5$ and $N_0 = 10$, the detection limit is purely determined by the photon and readout noise. For the case of $\gamma = 1.5$ and $N_0 = 100$, $\gamma = 2.5$, and $\gamma = 3.0$, both the source confusion and the other noises contribute to the detection limits. The combined detection limits for this case exceeds both the noise dominated result (table 2) and source confusion dominated result (table 4). In the case of $\gamma = 3.0$ and $N_0 = 60$, we cannot exactly determine the detection limits because the severe confusion makes the source detection difficult. Too many sources (i.e., $\gamma = 1.5$ and $N_0 = 100$, $\gamma = 3.0$ and $N_0 = 60$) also act as the large amount of the photon

Figure10a.ps

Figure10b.ps

Figure10c.ps

Figure10d.ps

Table 6. Detection limits for distributed point sources with photon and readout noise, taking account of the effects of the performance of the entire system, the brightness of the sky, the telescope emission, and the distribution of sources.

Band	$\gamma = 1.5$ $N_0^* = 10$ (mJy)	$\gamma = 1.5$ $N_0^* = 100$ (mJy)	$\gamma = 2.5$ $N_0^* = 10$ (mJy)	$\gamma = 3.0$ $N_0^* = 60$ (mJy)
WIDE-L	26	125	68	440
N170	66	135	115	442
WIDE-S	21	82	40	310
N60	49	92	63	280

* $N_0(> 100\,\mathrm{mJy})$. Number per square degree.

noise, which affects in raising the detection limit. Therefore, accurate photometry could be an additional important factor for approaching the theoretical confusion limit in these cases.

Matsuhara et al. (2000) analysed the ISO data obtained for the high density case ($\gamma = 3.0$ and $N_0 = 60$) from the fluctuation analysis method, which is different from our photometric method. Because they assumed that the fluctuation is mainly caused by unresolved faint point sources, they could count the number of sources, even in a low flux range.

5. Summary

We have written observing simulation software, 'FISVI', for an upcoming infrared survey mission, ASTRO-F. Utilizing this software, we have estimated the performance of the Far Infrared Surveyor (FIS) onboard ASTRO-F for ideal conditions. We can carry out scanning simulations with a reasonable amount of computing resources by introducing the Compiled PSF. The software can be used to generate virtual data sets for a data-reduction pipeline.

We estimated the detection limits under various circumstances. For the case of a non-crowded source distribution, the readout noise is usually more important than the photon noise for dark patches of the sky by a factor of 1.3 to 2.5. This means that the bright parts of the sky can be easily dominated by photon noise. The emission from the telescope is less than the interstellar background as long as the telescope temperature remains less than 6 K, but it could contribute significantly to the long-wavelength band if the temperature becomes larger than 6.5 K (see figure 4).

In crowded fields, source confusion becomes important in identifying sources. The detection correctness becomes smaller for fainter sources. We have defined the confusion limit in such a way that the number of correctly detected sources within a 20% error becomes larger than 70% of the number of detected sources from photometry. Such a definition of the confusion-dominated detection limit gives very similar values of the confusion limit based on a simple formula. The source confusion becomes larger than the detection limits by photon and read-

out noise only if the number of faint sources becomes much larger than a simple extension of the IRAS source counts down to around 10 mJy, assuming no luminosity or density evolution. Recent models of source counts based on ISO and SCUBA observations (Matsuhara et al. 2000; Dole et al. 2001; Franceschini et al. 2001; Pearson 2001), however, predict the source distribution that is subject to significant confusion at the longest wavelength band (WIDE-L). Other bands appear to be noise-limited. The source confusion also could change the slope in $\log N$–$\log S$ plots.

In this paper, we have made many simplifying assumptions concerning the sky conditions. The actual sky brightness varies from place to place. The overall statistics of the galaxy counts should be significantly influenced by irregularities of the sky backgrounds. Also, in order to understand cosmological effects, we will consider various types of SED, the luminosity function, and the redshift distribution. The current version of FISVI does not take into account more complicated behaviors of the detectors. These issues will be discussed in forthcoming papers.

Acknowledgment

Appendix 1.   Compiled PSF

A.1.1.   PSF Convolution

The PSF of ASTRO-F/FIS, including the entire optical path, was computed using the ZEMAX optical simulation software package (Focus Software, Inc.). The resulting PSF at $\lambda = 200\ \mu$m is shown in figure 11, together with a circular aperture Airy pattern. The difference between the simulated PSF and the Airy pattern is very small, but noticeable. The simulated PSF is slightly narrower than the Airy pattern, and the side-lobe is more significant. Since FIS detectors do not lie on the optical axis of ASTRO-F, the PSF is slightly elongated with an ellipticity of ~ 0.05, but we assume the circular PSF in the present simulations. Since the FIS covers a wide range of wavelengths, the PSFs have been computed from 40 to 200 μm at 5 μm intervals.

Using the simulated PSF, we first obtain the PSF-convolved image $I_{\lambda,i}$ on the focal plane at wavelength λ, contributed solely by the i-th point source:

$$I_{\lambda,i}(\boldsymbol{r}) = F_{\lambda,i}\, h_\lambda(\boldsymbol{r}; \boldsymbol{r}'_i) \tag{A1}$$
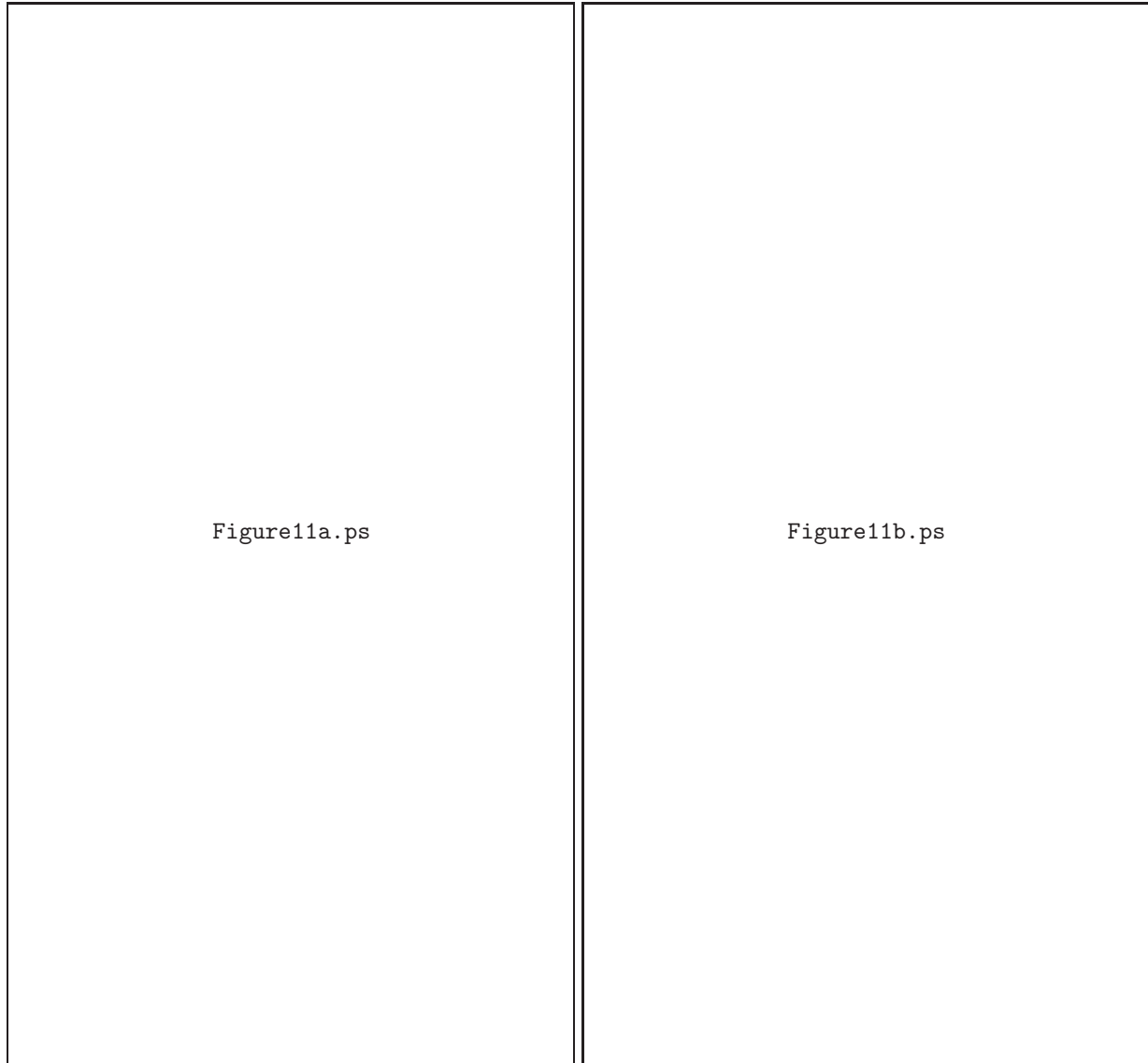
and

Figure11a.ps

Figure11b.ps

Fig. 11. PSF of the ASTRO-F/FIS at 200 μm in a linear scale (left panel) and a logarithmic scale (right panel). The solid line shows the PSF simulated by using ZEMAX and the dotted line shows the Airy pattern with the assumption of a single circular aperture system.

$$1 = \int_{\Omega} h_\lambda(\boldsymbol{r}; \boldsymbol{r}_i') \, d\Omega, \tag{A2}$$

where $\boldsymbol{r}$ is the position vector on the focal plane, $F_{\lambda,i}$ is the flux density (at the wavelength λ) of the i-th source, and $h_\lambda(\boldsymbol{r}; \boldsymbol{r}_i')$ is the simulated PSF at wavelength λ located centered at the position of the i-th source $\boldsymbol{r}_i'$. The PSF is normalised in such a way that the integration over the entire solid angle becomes unity. The intensity distribution on the focal plane, $I_\lambda(\boldsymbol{r})$, can then be obtained by

$$I_\lambda(\boldsymbol{r}) = \sum_i F_{\lambda,i} h_\lambda(\boldsymbol{r}; \boldsymbol{r}_i'). \tag{A3}$$

A.1.2. Filter Transmittance and Detector Response

As the detector sweeps the sky, it integrates the charge generated by photons that fall onto the detector. For a given intensity distribution on the focal plane, $I_\lambda(\boldsymbol{r})$, the power, $P_\lambda(\boldsymbol{r})$, at the wavelength interval $d\lambda$ is

$$P_\lambda(\boldsymbol{r})d\lambda = \int_{\Omega_{\mathrm{pixel}}} I_\lambda(\boldsymbol{r}) \, A_{\mathrm{tel}} \tau(\lambda) \, d\Omega d\lambda, \tag{A4}$$

where A_{tel} is the effective collecting area of the telescope, and $\tau(\lambda)$ is the filter transmittance along the photon path within FIS (Takahashi et al. 2000). The integration is performed over the solid angle subtended by the pixel.

The detector transforms the photons into charges. The total charge, D, integrated from t_1 to t_2 is

$$D(t_1 \rightarrow t_2) = \int_\lambda \int_{t_1}^{t_2} P_\lambda(\boldsymbol{r}(t)) \xi(\lambda) \, dt d\lambda, \tag{A5}$$

where $\xi(\lambda)$ is the detector response function in units of $\mathrm{A\,W^{-1}}$. We use the following convention:

$$\xi(\lambda) \equiv \xi_0 \tilde{\xi}(\lambda), \tag{A6}$$

where ξ_0 is a constant in units of $\mathrm{A\,W^{-1}}$ and $\tilde{\xi}$ is a function normalised to unity at the peak value for SW (short wavelength) and LW (long wavelength) detectors.

The normalised detector response functions, $\tilde{\xi}$, of LW and SW bands are shown in figures 12 and 13, respectively. We use these curves and the measured detector responsivity, ξ_{r}, to determine the normalisation constant, ξ_0. Measurements are done using a blackbody source, a filter that cuts off the photons below a certain wavelength, a Winston cone, and a detector in a perfectly reflecting cavity. The LW detector has long wavelength cut-off at 200 μm and SW detector at 110 μm. A low-pass filter was used to cut off the photons at wavelength below the FIS band. The short wavelength limits were 140 μm for the LW detector and 40 μm for the SW detector. The measured responsivity is represented by

$$\xi_r = \xi_0 \frac{\int_\lambda \tilde{\xi}(\lambda) \, B_\lambda(T) \, d\lambda}{\int_\lambda B_\lambda(T) \, d\lambda}, \tag{A7}$$

where $B_\lambda(T)$ is the Planck function at the temperature T. In this estimation, we use $T = 40$ K. From the measured value of $\xi_{\mathrm{r}} \approx 20 \, \mathrm{A\,W^{-1}}$ for LW, and $\xi_{\mathrm{r}} \approx 7 \, \mathrm{A\,W^{-1}}$ for SW, we can determine
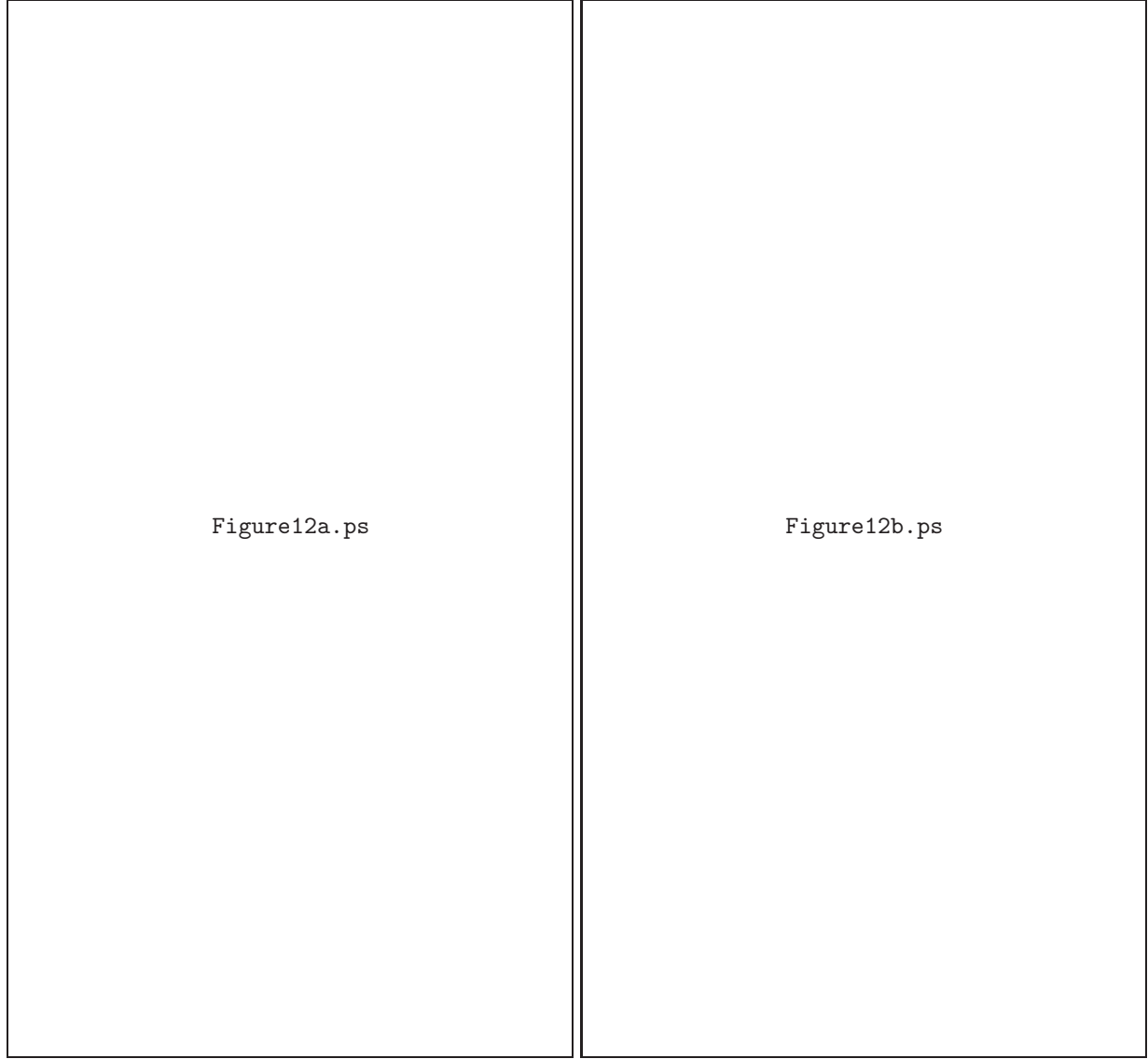
Fig. 12. Filter transmission, $\tau(\lambda)$, (dashed lines) and the detector's response function, $\tilde{\xi}(\lambda)$, (dotted lines) for the N60 band (left) and the Wide-S band (right). The combined responsivities are shown as solid lines in arbitrary units.

the normalisation constant, ξ_0. The normalisation constants are $\xi_0 = 30 \text{ A W}^{-1}$ for the LW and $\xi_0 = 10 \text{ A W}^{-1}$ for the SW detectors, respectively.

A.1.3. Compiled PSF

If we use the same spectral energy distribution (SED) for each source, the flux density of the source can be defined as

$$F_{\lambda,i} = \mathcal{F}_i \, S_\lambda, \tag{A8}$$

where S_λ is the spectral energy distribution (SED) normalised to unity over the wavelength band and $\mathcal{F}_i$ is the flux integrated over the bandwidth. We can rewrite equation (A3) as
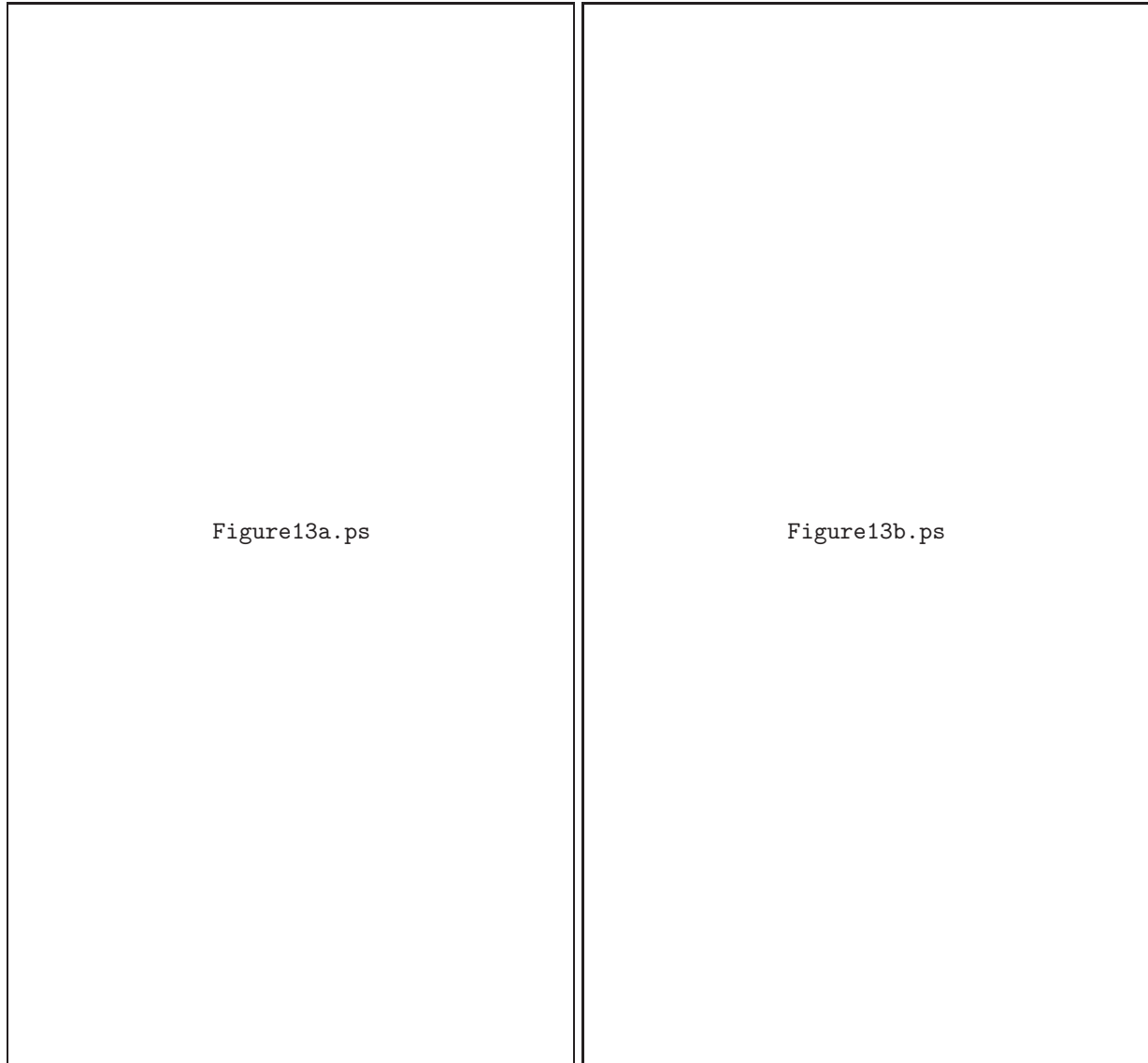
Figure13a.ps

Figure13b.ps

Fig. 13. Same as figure 12, except for the N170 band (left) and the WIDE-L band (right).

$$I_\lambda(\boldsymbol{r}) = \sum_i \mathcal{F}_i S_\lambda h_\lambda(\boldsymbol{r};\boldsymbol{r}_i'). \tag{A9}$$

Since λ is independent of $\boldsymbol{r}$ and $\boldsymbol{r}_i'$, we can introduce a new function, $H(\boldsymbol{r};\boldsymbol{r}_i')$, by integrating over the wavelength as

$$H(\boldsymbol{r};\boldsymbol{r}_i') = A_{\rm tel} \int_\lambda h_\lambda(\boldsymbol{r};\boldsymbol{r}_i') S_\lambda \tau(\lambda) \xi(\lambda) \; d\lambda. \tag{A10}$$

We define this $H(\boldsymbol{r};\boldsymbol{r}_i')$ as the 'Compiled PSF'. If we perform convolution to the image plane by using this Compiled PSF, we can avoid repeated wavelength integration. Finally, equation (A5) can be rewritten as

$$D(t_1 \to t_2) = \int_{t_1}^{t_2} \int_{\Omega_{\rm pixel}} \sum_i \mathcal{F}_i H(\boldsymbol{r};\boldsymbol{r}_i') \; d\Omega dt. \tag{A11}$$

This concept of the Compiled PSF is effective only when the number of SED type is limited. The calculation time is reduced by a factor of N_λ by using the Compiled PSF, where N_λ is the number of wavelength grids. With a wavelength interval of $\Delta\lambda = 5$ μm, a typical N_λ lies between 10 and 20. In order to carry out simulations over four square degrees in the WIDE-S band, we need about 15 hours of computing time with Pentium IV 1 GHz machines. By introducing Compiled PSF, we can accomplish such a simulation within an hour.

A.1.4. Spectral Energy Distribution of the Sources

We expect that the majority of faint point sources detected by the ASTRO-F/FIS will be external galaxies. Each object will have its own SED, but most extragalactic point sources in the infrared band can be classified into four types of galaxies, i.e., the cirrus type representing typical spiral galaxies, the M 82 type starbursts, the Arp 220 type starbursts and the AGN dust torus type (Rowan-Robinson 2001). Four Compiled PSFs are required to accommodate these four types of SEDs in the simulations. The observed SEDs are further affected by the redshifts. We need redshifted-dependent SEDs for each type of source.

We expect that the Compiled PSF will be changed with the SED types and the redshift for wide bands, but the difference was found to be very small, even for the WIDE-S and WIDE-L bands, as shown in figure 14. Since our main purpose is to examine the general performance of the ASTRO-F/FIS, we concentrate on simple models for the nature of the sources. We will deal with the SED types of sources, redshift distributions, and the luminosity function in the next paper in order to understand the cosmological model and the galaxy evolution through the observing simulation. Though the difference between the Compiled PSFs computed from the flat SED and other SEDs is severe at some extreme cases ($\sim 10\%$ difference over the area), we use the Compiled PSF computed for galaxies with the flat SED in the present paper (i.e., $F_\lambda = $ constant) (see figure 14). In the flat SED's case, the Compiled PSF does not depend on the redshift.
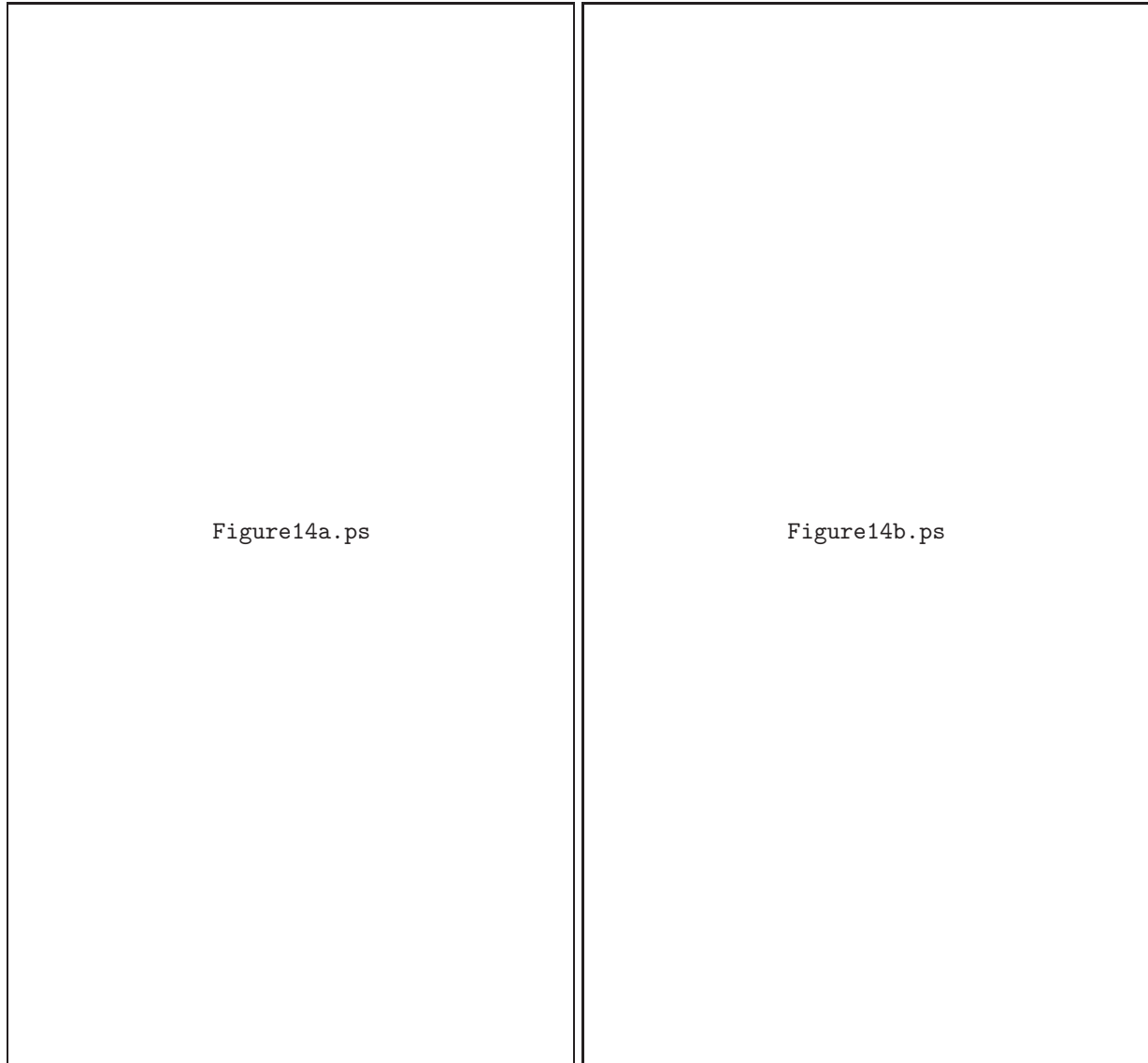
Figure14a.ps

Figure14b.ps

Fig. 14. Normalised Compiled PSFs in the WIDE-L band. The left panel is the Compiled PSFs over SED for redshift 1.0 and the right panel is the Compiled PSFs over redshift for the cirrus type. For a comparison, we also plot the Compiled PSF computed for galaxies with the flat SED used in this work.

Appendix 2.   Procedures of Scanning and Data Sampling

A PSF-convolved image is generated on grids where the scanning procedure is performed. To scan a PSF-convolved image, we need to know the position of the detector pixels. We set the array of the starting point to scan on the x (cross-scan direction) and the y (in-scan direction) frame in the image. The FIS detector arrays have 2 or 3 rows and 15 or 20 columns, and is tilted by an angle $\theta = 26.°5$ from the cross-scan direction in order to assure Nyquist sampling (Takahashi et al. 2000; Matsuura et al. 2001). We denote i as the index for the sampling sequence, and j and k as the indices for the row and column of the detector array, respectively (see figure 15). By denoting (x_0, y_0) as the position vector of the center of upper left pixel of the array at the beginning of the scan (i.e., $i = j = k = 0$), we have the following formulae for the position vectors of the (j, k) pixel at the $(i + 1)$-th sampling:

$$x(i, j, k) = x_0 + p(k \cos\theta + j \sin\theta) \tag{A12}$$

and

$$y(i, j, k) = y_0 + i v \Delta t + p(j \cos\theta - k \sin\theta), \tag{A13}$$

where p is the size of the pixel pitch (see table 1), v is the scanning angular speed (which is 3.60 arcmin s^{-1}) of the satellite, and Δt is the increment of the detector motion in the scan direction during the sampling interval. Note that the x position of each pixel does not depend on i in this coordinate system. We show one example for the passage of the detector in figure 16.

Appendix 3.   Integrating over the Detector Pixel

The integration of equation (A11) over Ω_{pixel} was carried out by summing up the image convolved with Compiled PSF on fine grids. The image convolved with Compiled PSF was constructed on grids of $4''$ resolution, but the accuracy of the Ω_{pixel} integration was not good enough on such grids ($\sim$ a few percent error), partly because of the tilted configuration of the detector arrays. In order to improve the accuracy of the integration, we laid finer grids over the area where the integration would be performed. We were able to reduce the integration error down to 1% by taking a three-times finer grid over the integration area. If we use a smaller grid, we can improve the accuracy of the flux and the position further, but we would need more computing time.

The time integration of equation (A11) was made by dividing one sampling interval to shorter subsampling intervals in order to mimic the continuous scanning of the detector and applying the trapezoidal rule to the subsampled time series data. As the detector moves, one detector pixel integrates the signal during the subsample interval (see figure 17). The number of subsample determines the resolution of integrated signal values. The sampling rate of 15.2 Hz for LW bands corresponds to $14.''2$ which is much smaller than the pixel size, and we found

Figure15.ps

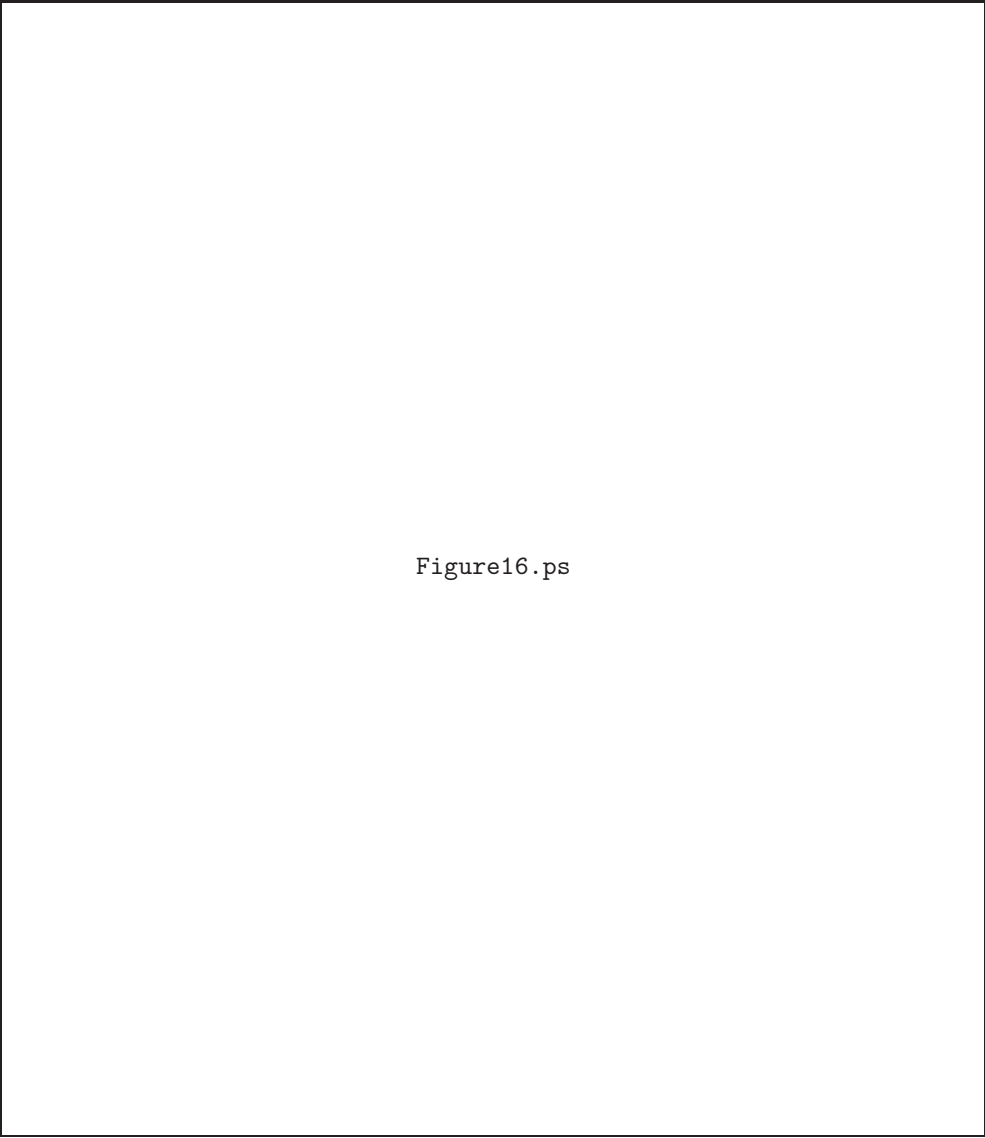**Fig. 15.** Layout of the detector array for the N170 band and definition of the scan directions.

Figure16.ps

Fig. 16. Passage of the detector for the WIDE-L band. We display the footprints of the detector pixels scanned three times.
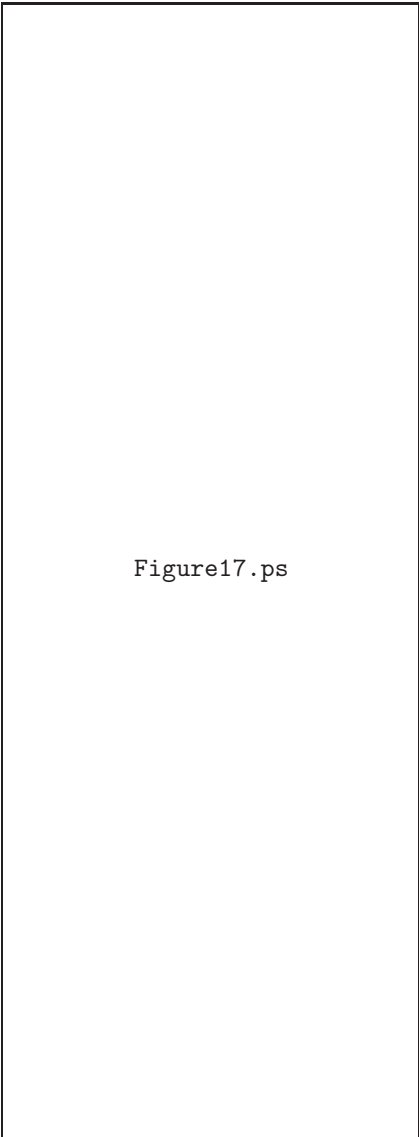
Fig. 17. Each sampling is composed of several subsamples in order to ensure accurate integration over the region where the intensity varies. s1–s5 mean the subsamples. In actual simulations, we used only two subsamples.

that we need only two subsamples to ensure the integration accuracy over time becomes smaller than 1%.

References

Bertin, E., & Arnouts, S. 1996, A&AS, 117, 393

Boggs, S. E., & Jean, P. 2001, A&A, 376, 1126

Condon, J. J. 1974, ApJ, 188, 279

Dole, H., et al. 2001, A&A, 372, 364

Efstathiou, A., et al. 2000, MNRAS, 319, 1169

Franceschini, A., Toffolatti, L., Danese, L., & De Zotti, G. 1989, ApJ, 344, 35

Franceschini, A., Aussel, H., Cesarsky, C. J., Elbaz, D., & Fadda, D. 2001, A&A, 378, 1

Garcia, R. A., Roca Cortés, T., & Régulo, C. 1998, A&AS, 128, 389

Herbstmeier, U., et al. 1998, A&A, 332, 739

Jeong, W.-S., et al. 2000, in Proc. of Mid- and Far-Infrared Astronomy and Future Missions, ed. T. Matsumoto & H. Shibai, ISAS Report, SP14, 297

Kawada, M. 1998, Proc. SPIE, 3354, 905

Kawada, M. 2000, in Proc. of Mid- and Far-Infrared Astronomy and Future Missions, ed. T. Matsumoto & H. Shibai, ISAS Report, SP14, 273

Kiss, C., Ábrahám, P., Klaas, U., Juvela, M., & Lemke, D. 2001, A&A, 379, 1161

Matsuhara, H., et al. 2000, A&A, 361, 407

Matsuura, M., Nakagawa, T., Murakami, H., & Yamamura, I. 2001, ISAS Report, 681, 1

Murakami, H. 1998, Proc. SPIE, 3356, 471

Nakagawa, T. 2001, in the Proc of The Promise of the Herschel Space Observatory, ed. G. L. Pilbratt, J. Cernicharo, A.M. Heras, T. Prusti, & R. Harris, ESA-SP, 460, 67

Pearson, C. P. 2001, MNRAS, 325, 1511

Puget, J. J., et al. 1999, A&A, 345, 29

Rieke, G. H. 1994, in Detection of Light: from the Ultraviolet to the Submillimeter, ed. K. Visnorsky (Cambridge: Cambridge University Press), pp. 65-67

Rowan-Robinson, M. 2001, ApJ, 549, 745

Shibai, H. 2000, in IAU Symp. 204, The extragalactic background and its cosmological implications, ed. M. Harwit & M. G. Hauser (Michigan: Astronomical Society of the Pacific), 455

Takahashi, H., et al. 2000, Proc. SPIE, 4013, 47

This figure "Figure01.ps.gif" is available in "gif" format from:

http://arXiv.org/ps/astro-ph/0204377v3

This figure "Figure02a.ps.gif" is available in "gif" format from:

http://arXiv.org/ps/astro-ph/0204377v3

This figure "Figure02b.ps.gif" is available in "gif" format from:

http://arXiv.org/ps/astro-ph/0204377v3

This figure "Figure03.ps.gif" is available in "gif" format from:

http://arXiv.org/ps/astro-ph/0204377v3

This figure "Figure04.ps.gif" is available in "gif" format from:

http://arXiv.org/ps/astro-ph/0204377v3

This figure "Figure05.ps.gif" is available in "gif" format from:

http://arXiv.org/ps/astro-ph/0204377v3

This figure "Figure06a.ps.gif" is available in "gif" format from:

http://arXiv.org/ps/astro-ph/0204377v3

This figure "Figure06b.ps.gif" is available in "gif" format from:

http://arXiv.org/ps/astro-ph/0204377v3

This figure "Figure07a.ps.gif" is available in "gif" format from:

http://arXiv.org/ps/astro-ph/0204377v3

This figure "Figure07b.ps.gif" is available in "gif" format from:

http://arXiv.org/ps/astro-ph/0204377v3

This figure "Figure07c.ps.gif" is available in "gif" format from:

http://arXiv.org/ps/astro-ph/0204377v3

This figure "Figure07d.ps.gif" is available in "gif" format from:

http://arXiv.org/ps/astro-ph/0204377v3

This figure "Figure08a.ps.gif" is available in "gif" format from:

http://arXiv.org/ps/astro-ph/0204377v3

This figure "Figure08b.ps.gif" is available in "gif" format from:

http://arXiv.org/ps/astro-ph/0204377v3

This figure "Figure08c.ps.gif" is available in "gif" format from:

http://arXiv.org/ps/astro-ph/0204377v3

This figure "Figure08d.ps.gif" is available in "gif" format from:

http://arXiv.org/ps/astro-ph/0204377v3

This figure "Figure09a.ps.gif" is available in "gif" format from:

http://arXiv.org/ps/astro-ph/0204377v3

This figure "Figure09b.ps.gif" is available in "gif" format from:

http://arXiv.org/ps/astro-ph/0204377v3

This figure "Figure09c.ps.gif" is available in "gif" format from:

http://arXiv.org/ps/astro-ph/0204377v3

This figure "Figure09d.ps.gif" is available in "gif" format from:

http://arXiv.org/ps/astro-ph/0204377v3

This figure "Figure10a.ps.gif" is available in "gif" format from:

http://arXiv.org/ps/astro-ph/0204377v3

This figure "Figure10b.ps.gif" is available in "gif" format from:

http://arXiv.org/ps/astro-ph/0204377v3

This figure "Figure10c.ps.gif" is available in "gif" format from:

http://arXiv.org/ps/astro-ph/0204377v3

This figure "Figure10d.ps.gif" is available in "gif" format from:

http://arXiv.org/ps/astro-ph/0204377v3

This figure "Figure11a.ps.gif" is available in "gif" format from:

http://arXiv.org/ps/astro-ph/0204377v3

This figure "Figure11b.ps.gif" is available in "gif" format from:

http://arXiv.org/ps/astro-ph/0204377v3

This figure "Figure12a.ps.gif" is available in "gif" format from:

http://arXiv.org/ps/astro-ph/0204377v3

This figure "Figure12b.ps.gif" is available in "gif" format from:

http://arXiv.org/ps/astro-ph/0204377v3

This figure "Figure13a.ps.gif" is available in "gif" format from:

http://arXiv.org/ps/astro-ph/0204377v3

This figure "Figure13b.ps.gif" is available in "gif" format from:

http://arXiv.org/ps/astro-ph/0204377v3

This figure "Figure14a.ps.gif" is available in "gif" format from:

http://arXiv.org/ps/astro-ph/0204377v3

This figure "Figure14b.ps.gif" is available in "gif" format from:

http://arXiv.org/ps/astro-ph/0204377v3

This figure "Figure15.ps.gif" is available in "gif" format from:

http://arXiv.org/ps/astro-ph/0204377v3

This figure "Figure16.ps.gif" is available in "gif" format from:

http://arXiv.org/ps/astro-ph/0204377v3

This figure "Figure17.ps.gif" is available in "gif" format from:

http://arXiv.org/ps/astro-ph/0204377v3